Optics Letters

Full-day profiling of a beam attenuation coefficient using a single-photon underwater lidar with a large dynamic measurement range

Mingjia Shangguan,* Zhifeng Yang, Zaifa Lin, Zhenwu Weng, and Jiaxin Sun

State Key Laboratory of Marine Environmental Science, College of Ocean and Earth Sciences, Xiamen University, Xiamen 361102, China
**mingjia@xmu.edu.cn*

Received 29 November 2023; revised 25 December 2023; accepted 25 December 2023; posted 2 January 2024; published 25 January 2024

A compact underwater lidar system, utilizing a single-photon detection technology, is proposed to effectively eliminate interference from the sea–air interface and enhance the accuracy of water optical property measurements. However, the high sensitivity of the single-photon detector poses challenges, including daytime operation difficulties due to strong solar radiation noise and detector saturation from near-field lidar signals. To address these issues, the laser and optical receiver of the lidar are optimized to suppress solar radiation noise, and a dual-telescope structure is introduced to improve the dynamic measurement range beyond 70 dB. In addition, a Monte Carlo simulation establishes the relationship between beam attenuation coefficients (c) and lidar attenuation coefficients (K_{lidar}), enabling the retrieval of c profiles from K_{lidar}. A field experiment conducted in the South China Sea, spanning from inshore to offshore waters, demonstrates the effectiveness of the lidar. The results highlight its potential applications, including the assessment of subsurface particulate organic carbon (POC).

https://doi.org/10.1364/OL.514622

Lidar technology has become integral for three-dimensional ocean remote sensing due to its deep penetration capabilities, exceeding passive ocean color remote sensing by threefold, and its ability to continuously profile the ocean day and night [1]. Its applications span various domains, including underwater topography detection [2], phytoplankton carbon assessment [3], observations of scattering layers [4], diel vertical migration of marine organisms [5], analysis of inherent optical properties (IOP) of water [6,7], and temperature measurement [8], among others. However, the air–sea interface interference presents a significant challenge for oceanic lidar systems [9]. This interference affects the detection depth of the lidar and modulates its backscattered signals, leading to challenges in accurate signal analysis and parameter retrieval, especially in instances of substantial sea surface fluctuations.

Deploying lidar systems underwater is a crucial step in mitigating air–sea interface interference [10,11]. However, successful underwater deployment requires the miniaturization and lightweight design of lidar systems. Single-photon detection technology has emerged as a promising solution, offering high-performance lidar detection using a low-energy laser and a small aperture telescope, making it well-suited for underwater lidar systems. Consequently, single-photon underwater lidars (SPULs) have found applications in detecting oil in water [11], bathymetry [12], bubbles [10], and imaging [13]. However, the high sensitivity of single-photon detectors presents two key technical challenges. Firstly, the operational wavelength of ocean detection lidar falls within the blue–green band, where solar radiation is strongest, posing difficulties for daytime operations [11]. Secondly, detector saturation resulting from strong near-field signals coupled with the limited dynamic measurement range affects detection depth.

Despite obtaining continuous day–night lidar backscattered signals with a large dynamic measurement range, profiling the beam attenuation coefficient (c), which is an optical measure for the decrease in light intensity per unit length due to absorption and scattering in water, remains challenging when using oceanic lidar systems. The c parameter is crucial in tracking the concentration of particulate organic carbon (POC), facilitating studies of the marine carbon cycle [14]. However, this task faces limitations in lidar platforms and the large lidar footprint, leading to significant multiple scattering components in lidar backscattered signals. Consequently, the inverted lidar attenuation coefficient (K_{lidar}), which is derived from lidar backscatter signals that incorporate a substantial amount of multiple scattering components, is typically associated with the diffuse attenuation coefficient (K_d) rather than c [15]. Fortunately, in the SPUL system, the inverted K_{lidar} demonstrates a correlation with c due to significant multiple scattering suppression. However, the relationship between SPUL's K_{lidar} and c remains insufficiently understood.

To address these challenges, a novel SPUL is proposed. To enable daytime operation, the lidar utilizes a narrowband laser and optical filter to suppress solar radiation noise in the spectrum domain. Additionally, single-photon detectors allow for a significant reduction in the aperture and FOV of the optical telescope, ensuring only radiation noise within a small solid angle enters the optical receiver. Furthermore, due to underwater operation, reflections at the air–water interface and the absorption and scattering effects of water further attenuate radiation noise entering the lidar.

To enhance the signal dynamic measurement range and detection depth of the SPUL, a separate transmit–receive configuration is employed with a dual-telescope design. The first

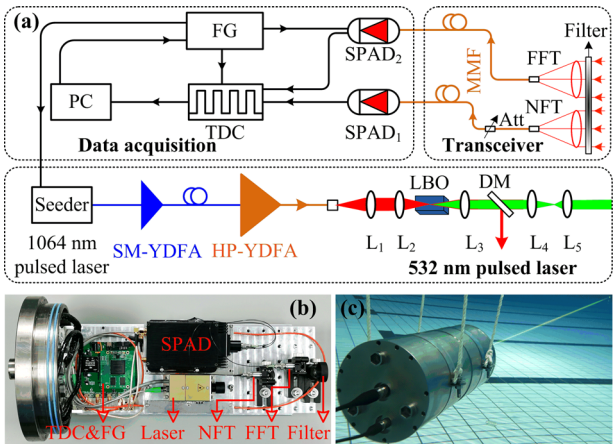

Fig. 1. (a) Schematic setup of the SPUL. SM-YDFA, single-mode ytterbium-doped fiber amplifier; HP-YDFA, high-power ytterbium-doped fiber amplifier; L, lens; LBO, lithium borate; DM, dichroic mirror; NFT, near-field telescope; FFT, far-field telescope; Att, fiber attenuator; MMF, multimode fiber; SPAD, single-photon avalanche diode; TDC, time-to-digital converter; FG, function generator; PC, personal computer. (b) Internal photo of the SPUL. (c) Photo of the SPUL.

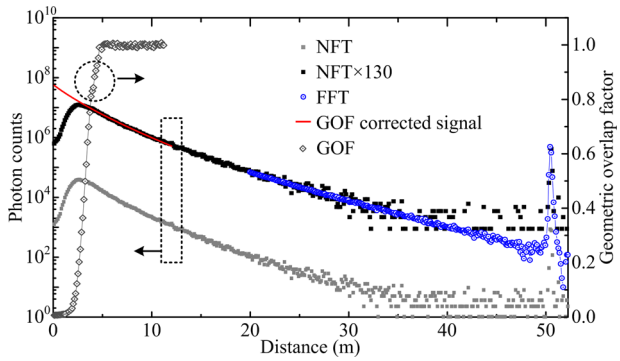

Fig. 2. Lidar-received backscattered signals, with solid gray rectangles depicting signals received by the NFT and blue circles representing signals received by the FFT. FFT-received signals within the first 20 m are isolated using gating control technology. Hollow black rectangles indicate the GOF calculated from NFT-received signals. The solid red line represents the near-field signal after GOF correction, and the solid black frame represents the signal after GOF correction multiplied by an attenuation factor of 130.

optical telescope, termed the near-field telescope (NFT), is used to detect near-field backscattered signals. Due to the effect of the geometric overlap factor (GOF), which defines the spatial coverage between the laser beam and the field of view (FOV) of the telescope, it effectively adjusts and mitigates strong near-field signals. Additionally, to ensure that the signal remains below the saturation count rate of the single-photon detector, the backscattered signal is attenuated by a factor of 130 in this work. Due to the proportional attenuation of solar radiation, it also leads to an improvement in the signal-to-noise ratio (SNR). The second optical telescope, known as the far-field telescope (FFT), specializes in detecting signals beyond a depth of 20 m. To isolate strong near-field signals, a gating technology is utilized. Ultimately, through the dual-telescope design, the SPUL achieves a dynamic range exceeding 70 dB. Finally, a Monte Carlo (MC) simulation for SPUL is employed to establish the relationship between c and K_{lidar}, enabling the retrieval of c profiles from K_{lidar} profiles.

The SPUL system setup, depicted in Fig. 1, includes a 532 nm pulsed laser, a transceiver, and a data acquisition system. The laser utilizes a compact fiber-based picosecond (ps) laser and a master oscillator power amplifier (MOPA) architecture. Starting at 1064 nm, the seed laser, which is a single-mode single-frequency pulsed laser, undergoes amplification via a single-mode ytterbium-doped fiber amplifier (SM-YDFA) and two-stage high-power ytterbium-doped fiber amplifiers (HP-YDFAs). A lithium borate (LBO) crystal facilitates second harmonic generation, yielding the desired 532 nm wavelength with an average output power of up to 1 W. Employing the MOPA architecture maintains a narrow linewidth of 0.04 nm for the 532 nm laser, with a pulse width of 501 ps, a beam divergence of 0.5 mrad, a beam diameter of 5 mm, a pulse repetition rate of 1 MHz, and an individual pulse energy of 1 μJ.

An all-fiber connection configuration is used in the optical receiver system for the SPUL, ensuring a compact and robust structure. The backscattered signal resulting from the interaction between the 532 nm laser and water is received by the dual-telescope system. Background noise is suppressed using a 1-in. 532 nm filter with a bandwidth of 0.08 nm before the telescope. The backscattered signals are coupled into a 105-μm multimode fiber (MMF) by the dual telescope (Thorlabs F220FC-532) with a 10.9 mm focal length, corresponding to a FOV of ~9.6 mrad. The NFT and the transmitted laser maintain a separation of ~6 mm, ensuring a 100% GOF at approximately 5 m. In contrast, the separation between the FFT and the transmitter is ~18 mm, with the GOF reaching 100% at around 10.5 m.

The signal received by the NFT is attenuated 130 times and then detected by a single-photon avalanche diode ($SPAD_1$), while the signal received by the FFT is directly fed into another $SPAD_2$. The single-photon detector has a detection efficiency of 52% at the 532 nm and maintains a dark count rate of 100 counts per second (cps). Subsequently, the output from the single-photon detector is linked to a dual-channel time-to-digital convertor (TDC) operating at a sample rate of 5 GHz. Regarding the electronic module, a custom-designed function generator (FG) built on a field-programmable gate array (FPGA) delivers precise control signals to the laser, TDC, and $SPAD_2$. The lidar boasts dimensions of 20 cm in diameter and 40 cm in length. With an average power consumption of approximately 80 W, the lidar has a weight of 15 kg.

To test the dynamic measurement range of the lidar and calculate the GOF for near-field signal, experiments were conducted in a laboratory pool at Xiamen University with dimensions of 50 m × 25 m × 1.8 m (length, width, depth). During the experiment, the lidar was horizontally positioned at a depth of 0.8 m underwater. During the data processing, the photon counts measured within 10 s were accumulated based on a range resolution of 5.6 cm. As shown in Fig. 2, it is observed that both NFT-received and FFT-received signals exhibit exponential decay after reaching the GOF of 1. This observation of uniform water mixing prompts the calibration of GOF. Taking signals measured by the NFT with a GOF of 1 (i.e., in the range of 6–12 m) involves computing the natural logarithm of the photon count (P) multiplied by the square of the distance (z), resulting in $\ln(Pz^2)$. By linearly fitting this $\ln(Pz^2)$ data, the signal at a GOF of 1 for 0–6 m is reverse-calculated, as depicted by the red line in

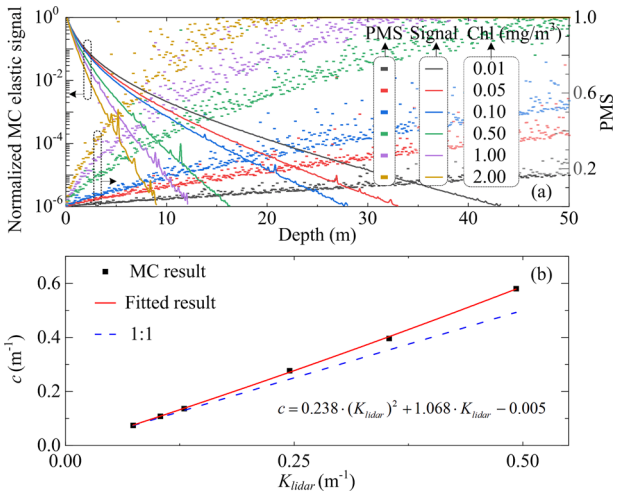

Fig. 3. (a) MC-simulated lidar signals at different Chl levels (solid lines) and the corresponding percentage of multiple scattering (PMS) in the signals (scatters). (b) Relationship between c and K_{lidar} derived from the simulated data in (a), with scatter representing MC simulation results, and the solid line denoting the fit using a binomial function.

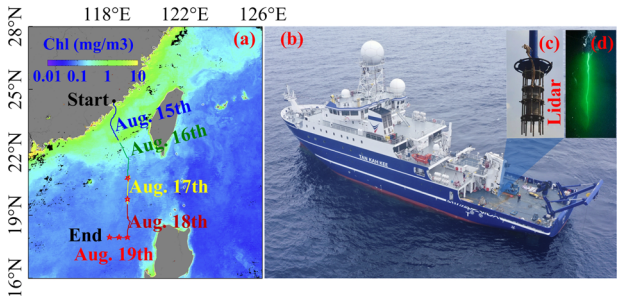

Fig. 4. (a) R/V navigation trajectory with lidar, overlaid on a monthly averaged Chl-a map from ocean color satellite. Red pentagon stars indicate R/V operation station positions. (b) Lidar installation on the R/V. (c) Installation process illustration. (d) Underwater operation of the lidar. Chl-a data sourced from NASA MODIS standard monthly composite for August 2023.

Fig. 2. Dividing the measured signal for 0–6 m by this reverse-calculated signal gives the GOF, illustrated by the hollow black rectangles in Fig. 2.

Furthermore, to prevent detector saturation caused by near-field signals received by the FFT, a function generator (FG) generates a TTL signal synchronized with the laser pulse and directs it to the $SPAD_2$, as shown in Fig. 2. It is worth noting that since the $SPAD_1$ is used to detect near-field signals, and these signals no longer saturate the $SPAD_1$, the gating control for the $SPAD_1$ is no longer necessary. The single-photon detector operates during the high TTL level while remaining inactive during the low TTL level. Following the emission of the laser pulse, a continuous TTL low-level signal lasting ~355 ns is applied to the detector, effectively isolating the near-field signals within the 0–20 m range. The detected results are shown by the blue circles in Fig. 2. The peak at approximately 51 m in the reflected signals is a consequence of the pool wall's reflection, which is situated beyond the length of the pool due to the laser beam being angled relative to the pool's longer side. Finally, as illustrated in Fig. 2, the SPUL is capable of simultaneously detecting strong near-field signals (exceeding 10^7 photons) and weak far-field signals (1 photon), thereby achieving a dynamic measurement range of over 70 dB. In the synthesized data of Fig. 2, the signal received by the NFT in the 20–40 m range closely resembles that received by the FFT in the same range, though with a slightly lower SNR in the NFT-received signal. Consequently, in subsequent experiments, the NFT is utilized to receive signals within the 0–20 m range, while signals beyond 20 m are captured using the FFT.

To establish the relationship between c and K_{lidar}, a semi-analytic MC method was employed. In the simulation, the scattering phase function employed the Petzold phase function, and instrument parameters were derived from the SPUL data. The bio-optical models used, which allow the determination of absorption and scattering coefficients based on chlorophyll concentrations (Chl), as well as the simulation process, were informed by the latest literature [7]. The simulated results in Fig. 3 illustrate that at low Chl, the proportion of multiple scattering (PMS) in the lidar signal is low as shown in Fig. 3(a). With an increase in Chl, the percentage of multiple scattering (PMS) signals in the lidar signal increases. However, as seen from the relationship established between c and K_{lidar} based on the simulated signals in Fig. 3(a), as shown in Fig. 3(b), when Chl is ≤ 2 mg/m^3, their relationship is generally on the 1:1 line. At low Chl levels, c closely aligns with K_{lidar}. However, with an increase in Chl, c moderately exceeds K_{lidar}. A binomial function provides a well-fitted relationship between the two parameters, achieving an R-squared value of 0.99.

To demonstrate the effectiveness and robustness of the SPUL, a field experiment was conducted aboard the R/V Tan Kah Kee in the South China Sea from August 15 to August 19, 2023. Figure 4(a) illustrates the navigation trajectory from inshore to offshore, with a background display of a monthly averaged Chl-a map from ocean color satellite data. During this period, a total of five station works was conducted, as indicated by the red pentagon stars in Fig. 4. The underwater lidar, depicted in Fig. 4(b), was installed in the moon pool of the R/V Tan Kah Kee, with a draft depth of 1.7 m. The lifting process of the underwater lidar fixed to the moon pool is demonstrated in Fig. 4(c). A photo of the SPUL operating underwater is shown in Fig. 4(d).

The profiles of subsurface c obtained through inversion during the entire navigation are shown in Fig. 5. Two data gaps occurred during the study: the first lasted for approximately 1 h, and the second for about 40 min, as indicated by the white gaps in Fig. 5. These gaps resulted from communication issues with the lidar. During data processing, photons were accumulated within 2-s intervals at depth intervals of 5.6 cm. Following the GOF correction, K_{lidar} was inverted using the slope method [16]. The relationship between c and K_{lidar}, depicted in Fig. 3, was then utilized for inversion to obtain the c profiles. From the figures, it is observed that in the inshore, c values are relatively high, with a detection depth of around 4.5 m. As the R/V moves toward the open sea, c values decrease, and simultaneously, the detection depth increases, reaching ~60 m. The noise received by the NFT is negligible during the daytime, thanks to a 130-fold attenuation. However, under clear and cloudless daytime conditions, the signals received by the FFT still exhibit solar radiation noise, resulting in a typical noise level of approximately 100 cps/bin/s and shallower daytime observations by about 10 m compared to nighttime observations. Additionally, by comparing lidar-retrieved c at 1.7 m with *in situ* turbidity and Chl measured by WET Labs ECO-FL(RT)D [17], as shown in

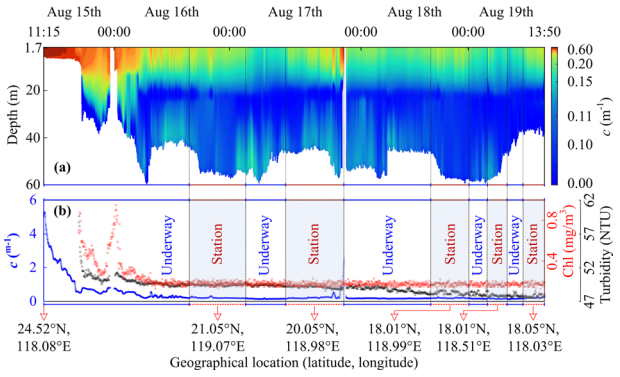

Fig. 5. (a) Lidar-observed subsurface c profiles. (b) Comparison between lidar-derived c data at a depth of 1.7 m and *in situ* measurements of Chl and turbidity.

Fig. 5(b), the trend of c aligns fundamentally with these two parameters. The primary disparity in trends arises from the distinct measurement locations of these two instruments: the *in situ* device measures the water surface, while lidar data is collected starting from a depth of 1.7 m.

In conclusion, a SPUL with a dynamic measurement range exceeding 70 dB was proposed and demonstrated for continuous profiling of the c throughout the day. Furthermore, due to the small laser beam and receiver aperture, the K_{lidar} closely approximated the c. In a field experiment conducted from inshore to offshore locations, the lidar successfully obtained profiles of c. In this study, the application of the slope method for K_{lidar} inversion has certain limitations. Looking ahead, more advanced approaches, such as high-spectral-resolution lidar technology, will be integrated into the SPUL to enhance the accuracy of K_{lidar} inversion. Ultimately, these research findings underscore the significant potential of lidar systems in remote sensing the IOPs of water bodies, providing crucial data for the study of POC, and advancing our deeper understanding of underwater environments.

Funding. Innovation Program for Quantum Science and Technology (2021ZD0303102); National Key Research and Development Program of China (2022YFB3901704); Fujian Provincial Central Guided Local Science and Technology Development Special Project (2022L3078); Joint Funds of the National Natural Science Foundation of China (U2106210); MEL-RLAB Joint Fund for Marine Science & Technology Innovation.

Acknowledgment. We acknowledge the captain and crew of the R/V Tan Kah Kee for their help during the cruises, particularly Guanggao Xu, Peng Wang, Chengmiao Ye, Xuewen Wu, Jing Dong, and Jiannan Cai. *In situ* Chl data were collected onboard R/V Tan Kah Kee of Xiamen University implementing the open research cruise NORC2023-06 supported by the NSFC Shiptime Sharing Project (project number: 42249906).

Disclosures. The authors declare no conflicts of interest.

Data availability. The data that support the findings of this study are available from the corresponding author upon reasonable request.

REFERENCES

1. C. Jamet, A. Ibrahim, Z. Ahmad, *et al.*, Front. Mar. Sci. **6**, 251 (2019).
2. Y. Ma, N. Xu, Z. Liu, *et al.*, Remote Sensing of Environment **250**, 112047 (2020).
3. J. A. Schulien, M. J. Behrenfeld, J. W. Hair, *et al.*, Opt. Express **25**, 13577 (2017).
4. J. H. Churnside and P. L. Donaghay, ICES J. Mar. Sci. **66**, 778 (2009).
5. M. J. Behrenfeld, P. Gaube, A. Della Penna, *et al.*, Nature **576**, 257 (2019).
6. M. Shangguan, Z. Liao, Y. Guo, *et al.*, Opt. Express **31**, 25398 (2023).
7. M. Shangguan, Y. Guo, Z. Liao, *et al.*, Opt. Express **31**, 40393 (2023).
8. Y. Wang, J. Zhang, Y. Zheng, *et al.*, Opto-Electron. Adv. **6**, 220016 (2023).
9. X. Shen, W. Kong, P. Chen, *et al.*, Remote Sens. **14**, 3351 (2022).
10. M. Shangguan, Z. Yang, Z. Lin, *et al.*, IEEE Geosci. Remote Sensing Lett. **20**, 1 (2023).
11. M. Shangguan, Z. Yang, M. Shangguan, *et al.*, Appl. Opt. **62**, 5301 (2023).
12. M. Shangguan, Z. Weng, Z. Lin, *et al.*, Opt. Express **31**, 43950 (2023).
13. A. Maccarone, K. Drummond, A. McCarthy, *et al.*, Opt. Express **31**, 16690 (2023).
14. Y. Ma, K. Zhou, W. Chen, *et al.*, Biogeosciences **20**, 2013 (2023).
15. F. Corcoran and C. E. Parrish, Photogramm Eng. Remote Sensing **87**, 831 (2021).
16. J. H. Churnside, J. W. Hair, C. A. Hostetler, *et al.*, Remote Sens. **10**, 2003 (2018).
17. Y. Yamashita, C.-J. Lu, H. Ogawa, *et al.*, Mar. Chem. **177**, 298 (2015).